

Diffraction imaging of crystals with focused x-ray beamsA. Kazimirov,^{1,*} V. G. Kohn,² and Z.-H. Cai³¹*CHESS, Cornell University, Ithaca, New York 14853, USA*²*Russian Research Center "Kurchatov Institute," 123182 Moscow, Russia*³*Advanced Photon Source, 9700 S. Cass Avenue, Argonne, Illinois 60439, USA*

(Received 18 January 2010; revised manuscript received 19 May 2010; published 15 June 2010)

We describe an imaging technique based on diffraction of a focused x-ray beam in crystals. A focused beam is formed by a zone plate and Bragg diffracted from a crystalline sample positioned between the zone plate and the focus. The intensity pattern is recorded by a high-resolution charge-coupled-device detector placed in the focus. Diffraction images recorded from perfect Si and GaAs crystals for various reflections demonstrate the broadening of the focused beam due to a finite scattering length. The images from semiconductor epitaxial films and heterostructures show additional peaks originating from the interfaces with their spatial position corresponding to the depth from the surface. Diffraction images from isolated defects in Si crystal demonstrate capabilities to study bulk defects. Theoretical simulations for perfect crystals show excellent agreement with experiments. We demonstrate that the new imaging technique is depth sensitive and combines structural sensitivity of traditional x-ray topography methods with spatial in-plane resolution provided by focusing.

DOI: [10.1103/PhysRevB.81.214112](https://doi.org/10.1103/PhysRevB.81.214112)

PACS number(s): 61.05.C-, 41.50.+h

I. INTRODUCTION

Diffraction of a spatially confined x-ray beam from perfect crystals has been the subject of extensive theoretical analysis in the past (see Ref. 1, and references therein). In the case of Bragg diffraction, for a point source located on the surface of a crystal, an analytical expression describing the amplitude of the diffracted wave on the exit surface (which is, for the Bragg case, also the entrance surface) as a function of a spatial coordinate along the surface has been derived.²⁻⁴ Interesting physical effects have been discovered. It was found that for a sufficiently thin crystal the spatial intensity distribution of the diffracted beam is localized in two peaks: the first one corresponds to diffraction from the front surface and the second one originates from the back surface of the crystal. It was found also that the first peak is broadened by diffraction and, even for an infinitely narrow incident beam, it has a width of at least a few microns. These theoretical predictions have never been confirmed experimentally due to the obvious reason: it was impractical in a real experiment to place both a narrow slit and a detector (or a film) at the same location on the crystal surface. This is in a striking contrast with the Laue case in which the intensity pattern on the exit surface predicted by theory for a narrow incident beam has been studied in detail experimentally. These studies led to the development of x-ray section topography which is capable of providing depth information about defects in the bulk (see Ref. 1, and references therein).

It was shown recently^{5,6} that the physics of Bragg diffraction of a focused beam produced by modern focusing optics (e.g., refractive lenses) is very similar to the diffraction of a narrow beam produced by a narrow slit and the intensity patterns recorded at the focus shows all the features described above. It was also shown that the spatial pattern does not depend on the position of the crystal between the focusing optics and the focus. As in the case of a very narrow beam produced by a slit, the pattern produced by a focused beam shows the same two peaks, originating from the front

and the back surfaces and, for a perfect crystal, due to destructive interference, there is no intensity in between. It was demonstrated by computer simulations⁶ that any interface (or, defect, for the same reason) can break up this interference and will show up as additional intensity peaks. This property serves as a basis for a proposed new diffraction imaging technique, a "truly" sectional topography in the Bragg case. Indeed, the effective size of the beam "sectioning" the sample and producing the image is determined by focusing optics which nowadays, at the third generation synchrotron sources, can routinely provide 100 nm beams. The illuminating area can be zoomed in and out within the limits of a particular setup providing additional flexibility.

First experiments were performed on silicon-on-insulator samples with different thickness of the top layer and used a phase zone plate (ZP) as a focusing optic. The results fully confirm theoretical predictions: the broadening of the beam was observed and the peaks from the back surface of 4.5–25 μm thick Si layers were recorded.^{7,8} Additional intensity peaks due to the strain gradient introduced in the top layer during the bonding process were also observed, confirming the structural sensitivity of a new imaging technique to crystal defects and imperfections. In a more recent work,^{9,10} the detailed comparison of theory with experiment was performed on perfect thick and thin crystals using refractive lenses as focusing optics. Remarkable changes in the intensity patterns were observed as the crystal was rotated away from the exact Bragg position and the diffraction conditions changed from dynamical to kinematical.

In this paper, we describe in detail an imaging technique and report recent experimental results obtained from bulk crystals and layered crystalline structures that illustrate the basic principles and imaging capabilities. Experimental setup using a phase zone plate is described in next section. In Sec. III, we present a theoretical background and outline the computational approach applied to model experimental intensity patterns. In the next section, experimental images from perfect crystals using strong and weak Bragg reflections clearly demonstrate the broadening of the focused beam due to the

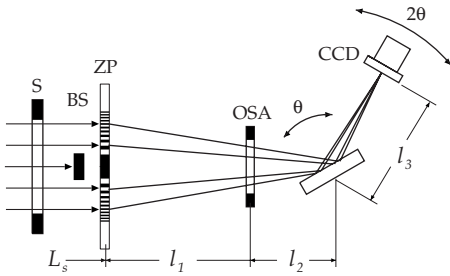


FIG. 1. Experimental setup: S slit in front of the zone plate ZP, BS—beam stop, OSA—order sorting aperture. High-resolution CCD camera is mounted on a 2θ arm of a six-circle diffractometer in the focus of the zone plate so that $l_1+l_2+l_3=L_f$. Sample is mounted on a θ axis and positioned between the zone plate and the focus.

extinction effect. Diffraction images from an epitaxial film and a multilayer structure grown by the molecular-beam epitaxy (MBE) on GaAs(001) substrate are presented and discussed in Sec. V. Images from individual defects in silicon crystal are discussed in Sec. VI followed by conclusions and outlook.

II. EXPERIMENTAL SETUP

Experiments were performed at the beamline 2-ID-D at the Advanced Photon Source, Argonne National Laboratory. This is a diffraction microscopy beamline based on a hard x-ray Fresnel zone-plate microprobe and a precise six-circle diffractometer.¹¹ The setup is shown schematically in Fig. 1. An x-ray beam from the APS undulator, tuned to the energy of 10.1 keV by a standard double-crystal Si(111) monochromator, is incident on a circular gold phase ZP with an outermost zone width of $0.1 \mu\text{m}$ located at the distance $L_s = 74 \text{ m}$ from the source. The slit S limits the size of the incident beam to the zone-plate aperture of $150 \mu\text{m}$. The focal distance at 10.1 keV is $l_1+l_2+l_3=13 \text{ cm}$. The $35\text{-}\mu\text{m}$ -diameter beam stop (BS) blocks the central part of the beam and the $25\text{-}\mu\text{m}$ -diameter order sorting aperture (OSA) located at the distance of l_1 from the ZP reduces the background contribution from the higher-order focusing. The size of the beam at the focus was $0.2 \mu\text{m}$.

A crystalline sample is mounted on a θ axis of a six-circle diffractometer on a sample holder equipped with precise XYZ nanopositional translation stages. A charge-coupled-device (CCD) camera (Princeton Scientific) is mounted on a 2θ (detector) arm and brought to the position of $l_3=8 \text{ mm}$ from the θ axis (the sample position). Then, the whole diffractometer is translated upstream to bring the surface of a scintillator crystal of the CCD camera to the focus of the zone plate. The full width at half maximum (FWHM) of the point spread function of the CCD camera was experimentally measured by imaging the focused beam to $1.5 \mu\text{m}$. A typical distance between the OSA and the CCD camera in our experiment is $l_2+l_3=13 \text{ mm}$. It is easy to estimate that, with the aperture of the zone plate of $150 \mu\text{m}$ and the sample-to-focus distance of 8 mm , the size of the beam incident on the sample surface is about $10 \mu\text{m}$. This value is limited by the

sample size and the focal distance and can be significantly reduced well below submicrometer level by downsizing a sample and choosing a focusing optics with a longer focal distance.

The CCD images were taken in two modes. In an angular scanning mode θ - 2θ scans were performed while taking images at each angular position through a Bragg diffraction region of the sample. Epitaxial structures usually exhibit several diffraction peaks corresponding to the layers of a different lattice constant (composition). As we demonstrate below (Sec. V), the diffraction images change dramatically depending on which diffraction peak is selected by the zone-plate angular aperture. By tuning the angle relative to the angular aperture a contrast of a selected layer can be enhanced. After a proper angle is chosen and fixed, the images can be taken while scanning the sample relative to the beam. This type of scan is presented in Sec. VI in which an isolated defect region in an annealed single silicon crystal is presented.

III. THEORETICAL BACKGROUND

Computer simulations of a two-dimensional x-ray wave field propagation through free space and optical devices present complex computational problems even for modern computers. Fortunately, in our experimental scheme the main optical device, namely, the crystal in the two-beam diffraction position, disturbs the wave field only in the (x, z) scattering plane, where the coordinate axis z is along the beam propagation, and the axis x is normal to it. Therefore, in this work we restrict ourselves to considering the intensity distribution only in the plane (x, z) at $y=0$. In a two-dimensional (x, y) intensity pattern, the line $y=0$ is a line of symmetry where the y derivative of a wave field equals zero. This line corresponds to the central cross section of experimentally recorded images by the diffraction plane. Taking into account an approximation of geometrical optics, it is easy to understand that the calculation of intensity distributions in one-dimensional cases is a good approximation which allows for a direct comparison of theoretical simulations with experimental data. Excellent agreement of theory with experiment for perfect crystals validates this approximation. Below we describe the theoretical approach used as a basis for the computational procedure utilized in this work.

It is well known that the propagation of a wave field in free space on some distance along the beam can be taken into account by means of a convolution of an incoming wave field with a free space propagator, known as the Kirchhoff propagator

$$P(x, z) = \frac{1}{(i\lambda z)^{1/2}} \exp\left(i\pi \frac{x^2}{\lambda z}\right), \quad (1)$$

where λ is the wavelength of monochromatic radiation.

We consider a crystal as a plate of some thickness and assume that this plate can only be inhomogeneous in the direction normal to the crystal surface; it is homogeneous along the surface within the footprint of the incident beam. At the Bragg condition this crystal reflects the incident plane wave into a new plane wave with the same wavelength but different direction. This means that the reflection of a spa-

tially inhomogeneous beam can be calculated as a convolution of an incoming wave field with a crystal propagator. The crystal propagator, by definition, is the response of a crystal to a point x-ray source (e.g., a very narrow slit) placed at its entrance surface. The crystal propagator is our main interest because it describes the transformation of an initially very narrow beam due to diffraction.

The most common way to calculate diffraction in crystals is based on solving Takagi equations. However, this set of differential equations in the Bragg case of diffraction is not easy to solve (so-called hard set) especially for a thick crystal. An alternative method is to consider a multilayer crystal in which each layer is perfect and uniform, whereby the diffraction from each layer has an analytical solution. All changes in the crystal structure take place at the layer boundaries. In this way the propagator of the multilayer crystal takes the following form:

$$P_{MC}(x) = \int \frac{dq}{2\pi} \tilde{P}_{MC}(q) \exp(iqx). \quad (2)$$

The propagator $P_{MC}(x)$ is the main goal of our analysis. The function $\tilde{P}_{MC}(q)$ is a response of a multilayer crystal on a plane wave. Theoretical problem of diffraction in a crystal composed of many crystalline layers has been the subject of many works. In our calculations we use a computational approach based on a recurrent formula derived in Ref. 12 (see references therein for some earlier works). For a crystal consisting of N layers the function $\tilde{P}_{MC}(q)$ can be calculated by applying N times the following formula connecting the reflection amplitude $R_k(q)$ for a crystal consisting of k layers with the reflection amplitude $R_{k-1}(q)$ for $k-1$ layers,

$$R_k(q) = \frac{R_1 - R_2 C \exp(i\varphi)}{1 - C \exp(i\varphi)}, \quad C = \frac{R_1 - R_{k-1}(q)}{R_2 - R_{k-1}(q)},$$

$$\varphi = \frac{ad_l}{\sin \theta_B}, \quad a = (\sigma^2 - s^2 f)^{1/2}, \quad R_{1,2} = \frac{\sigma \pm a}{sf}, \quad (3)$$

where the parameter $\sigma = (q - q_0) \sin(2\theta_B) - i\mu_0$ describes a deviation from the Bragg condition for a partial q plane wave, the parameter $s = K\chi_h$ describes the strength of the diffraction, $f = \chi_{-h}/\chi_h$ equals unity for crystals with inversion center, $\mu_0 = K \operatorname{Im}(\chi_0)$ is the linear absorption coefficient. The d_l is the layer thickness and $\chi_0, \chi_h, \chi_{-h}$ are the 0, $h, -h$ Fourier components of the susceptibility of the crystal lattice in the layer with the corresponding reciprocal-lattice vectors. The formulas are written for the symmetric case of diffraction, θ_B is the Bragg angle.

The parameter $q_0 = K[\varphi + (\Delta d/d) \tan \theta_B]$ describes a deviation from the Bragg condition due to a small rotation of the crystal by the angle φ from the Bragg position and a small relative change in the crystal lattice constant $\Delta d/d$. Because for an inhomogeneous incident beam the Bragg position is not very well defined, in the following we consider it relative to the center of the angular range. The crystal propagator does not depend on z because the transformation of the beam occurs at the entrance surface.

The other elements of the experimental scheme such as the beam stop, the zone plate, and the OSA influence the beam in a point-by-point manner. The propagator for each of these devices P_d can be written as $P_d(x) = T_d(x) \delta(x - x')$, where $\delta(x)$ is the Dirac delta function. The wave field transformation can be described by multiplication of the incident wave field amplitude by the factor $T(x) = A(x) \exp[iB(x)]$, which is called a transmission function. Because of the one-dimensional nature of our problem we replace circular objects by linear ones. The beam stop and OSA influence the amplitude $A(x)$ while the zone plate affects the phase $B(x)$. The first zone-plate radius r_1 determines the first-order focal length as $F = r_1^2/\lambda$.

The calculating scheme for the setup with the zone plate, Fig. 1, can be formally described as a set of convolutions,

$$E(x) = P(x, l_3) * P_{MC}(x) * P(x, l_2) * P_{OSA}(x) * P(x, l_1) * P_{ZP}(x) * P_{BS}(x) * P(x, L_s). \quad (4)$$

We start from a point source because various points on the source are incoherent. First, we determine the wave field traveled by the long distance L_s from the source to the zone plate. We ignore the distance between the BS and the ZP and consider modification of the wave field by both devices as taking place at the same position. Then we calculate the convolution due to a propagation on the distance l_1 between the ZP and OSA (see Fig. 1), account for a modification of the field by the OSA, and so on. We note that the beam stop, the zone plate and the OSA are taken into account by means of a simple multiplication by their transmission functions. Other convolutions are calculated by means of a double Fourier transformation technique by using fast Fourier transformation procedure.

Let us consider now a more simple setup with a refractive lens instead of a zone plate. This setup does not have any beam stops or OSAs and we use the propagator P_{PL} for a parabolic lens. In this case the scheme can be written as

$$E(x) = P(x, l_3) * P_{MC}(x) * P(x, l_1 + l_2) * P_{PL}(x) * P(x, L_s). \quad (5)$$

Here we used a well-known property of the Kirchhoff propagator $P(x, l_1) * P(x, l_2) = P(x, l_1 + l_2)$. If the detector is placed at the focus, i.e., at the distance of the imaging of the point source, then we can use a permutation property of the convolutions and write

$$E(x) = P_{MC}(x) * P(x, l_1 + l_2 + l_3) * P_{PL}(x) * P(x, L_s) \approx P_{MC}(x). \quad (6)$$

Derivation of the last expression is based on the fact that for a point source an ideal lens with infinite aperture focuses x rays to a point, therefore the source as δ function will have an image as δ function too. Then, convoluted with P_{MC} , we obtain the same function P_{MC} in the focus. Because the real lenses have finite aperture this expression is approximate. However, the better the focusing, i.e., the smaller the size of the beam at the focus, the better this approximation. Therefore, in this setup we have a unique possibility to visualize function P_{MC} in real space. This technique can be considered

as complementary to high-resolution diffraction in which the function $\tilde{P}_{MC}(q)$ is measured in reciprocal space. The situation with the zone plate is more complicated because the zone plate has multiple orders of focusing. However, using the BS and the OSA can significantly reduce their effects on the image at the focus. In this work we will apply computer simulations based on Eq. (4) for the setup on Fig. 1.

IV. PERFECT CRYSTALS: VISUALIZATION OF THE EXTINCTION EFFECT

Extinction of x rays in perfect crystals is one of the most important consequences of dynamical diffraction theory. Theory predicts that within the total reflection region of the Bragg diffraction the penetration of x rays in crystals is limited by a shallow surface layer and not by a photoelectron absorption length as one may expect.¹ In the center of the Bragg diffraction region the extinction length, which is by definition is the depth at which the amplitude of the plane wave is attenuated e times, is $L_{ex}=2 \sin \theta_B / (K|\chi_h|)$. For a given crystal material and x-ray energy the extinction length strongly depends on a chosen reflection and varies from about one micron for low-order reflections to few tens microns or more for higher-order reflections.

Extinction effect manifests itself in many diffraction phenomena. The most clear example is the dramatic drop in the fluorescence yield from the bulk atoms within the Bragg diffraction region.¹³ The fluorescing atoms act as detectors to measure the intensity of the x-ray field inside the crystal and a sharp decrease in the fluorescent yield indicates diminishing penetration depth. This effect is well known in a standing-wave method and is the main obstacle to localizing of bulk impurity atoms in crystals using this technique.

As was shown theoretically^{3,6} the extinction is responsible for the broadening of a focused beam by Bragg diffraction. In the spatial structure of the focused beam diffracted from perfect crystals the width of the peak corresponding to the front surface of the crystal is $2L_{ex} \cos(\theta_B)$, i.e., it is determined entirely by extinction. Therefore, using the technique presented in this paper we have a unique opportunity to visualize extinction effects and experimentally measure extinction length in a most direct way.

This theoretical prediction was confirmed experimentally⁹ using the x-ray beam focused by a planar refractive lens array to the size of $0.92 \mu\text{m}$ and the Si(111) reflection. In this work we studied diffraction images from perfect Si and GaAs crystals recorded using much smaller, round beams and using reflections of different orders from the same crystal. In Fig. 2(a) one can see the diffraction image from the Si(111) reflection (inset) and its cross section in the diffraction plane. The extinction length for this reflection is $1.50 \mu\text{m}$. Solid line is the theoretical curve calculated by applying the computational approach presented in Sec. III. The detector resolution was modeled by a Gaussian function with the FWHM as the only fitting parameter (except for the intensity scaling factor). The best fit gives the resolution of $1.4 \mu\text{m}$ and this parameter was fixed for all following calculations. In Fig. 2(b), the Si(333) diffraction image and its cross section are shown in the same scale. The extinction

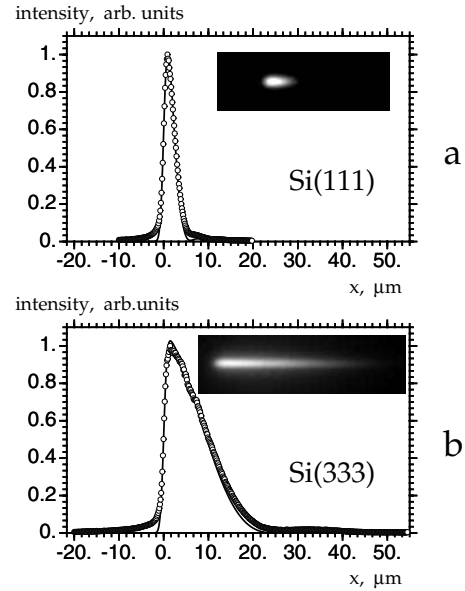


FIG. 2. Central cross sections of the diffraction images of the focused beam in diffraction plane recorded from a perfect Si crystal by using (a) the (111) and (b) the (333) reflections. The experimental images are shown as insets.

length for this reflection is $L_{ex}=7.82 \mu\text{m}$, solid line is the theoretical calculation, this time without any fitting parameters. As one can clearly see, the image is elongated in the diffraction plane due to extinction while in the direction perpendicular to the diffraction plane it is still well focused (the spot size determined by the detector resolution). The image is highly asymmetrical: while the left side of the peak is sharp and determined by the size of the beam at the focus (convoluted with the detector resolution), the right side is determined by the depth of the scattering layer.

Similar results for the GaAs(004) and (002) reflections are shown in Fig. 3. For this crystal the (004) reflection is the strong one with the Ga and As atoms scattering in phase and the extinction length is $1.66 \mu\text{m}$. The (004) image and its cross section is shown in Fig. 3(a). The (002) reflection is much weaker because the Ga and As atoms scatter out of phase, and the extinction length $L_{ex}=9.45 \mu\text{m}$, Fig. 3(b). Theoretical simulations (solid line) show excellent agreement with the experiment. One of the interesting future experiments would be to record diffraction images while scanning the energy of the incident beam across the Ga and As absorption edges and measure the scattering length as a function of energy.

V. IMAGING SEMICONDUCTOR STRUCTURES

Advances in semiconductor technology have been the major driving force for the development of modern x-ray diffraction characterization techniques including x-ray topography methods.¹⁴ Epitaxial films and multilayer structures remain the main building blocks of microelectronic and optoelectronic devices. In this section, we present first diffraction images obtained from an epitaxial film and a multilayer structure grown by the MBE technique.

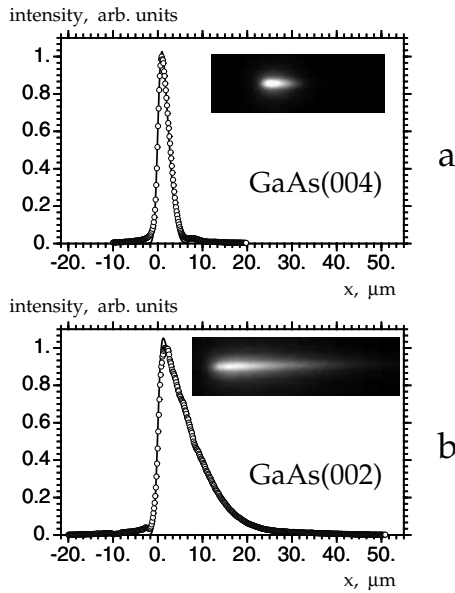


FIG. 3. Central cross sections of the diffraction images of the focused beam recorded from a perfect GaAs crystal by using (a) the (004) and (b) the quasiforbidden (002) reflections. The experimental images are shown as insets.

A. $Al_{0.7}Ga_{0.3}As$ epitaxial film on GaAs(001)

Thick $Al_{0.7}Ga_{0.3}As$ epitaxial film was grown on the GaAs(001) substrate by the MBE technique with the growth rate of 1 monolayer/s. Due to the compositional difference the x-ray rocking curves for this sample show two diffraction peaks, one from the substrate and the second, stronger one, from the film shifted by -1.75 mrad for the (004) reflection and -0.81 mrad for the (002) reflection relative to the substrate peak. With the angular aperture of the zone plate of 1.15 mrad we have an additional opportunity to select one of the two diffraction peaks.

The (004) and (002) experimental diffraction images and their cross sections are shown in Fig. 4. The surface of the film and the interface between the film and the substrate are clearly seen in all three images as separate diffraction peaks, though the visibility of these peaks and their intensity are different depending on the chosen reflection and the angular position. By measuring the distance between the peaks from the surface and from the interface the thickness of the film can be determined as $7.1 \mu m$. The schematic of the sample, i.e., the relative lattice-constant difference as a function of the distance from the surface, is shown in Fig. 4(a).

Theoretical simulations were performed for the experimentally determined thickness and the diffraction parameters corresponding to the film composition. Theoretical curves for the perfect film and uniform composition are shown on all three profiles as thin lines. As one can see, the shape of the first peak and the depth position of the second peak are very well reproduced but the shape of the second peak which corresponds to the interface is not. Also, additional intensity originating from the bulk of the film is clearly observed.

As was described in Sec. II the computational algorithm can be applied to a multilayer crystal in which each layer has a perfect lattice with its own diffraction parameters which

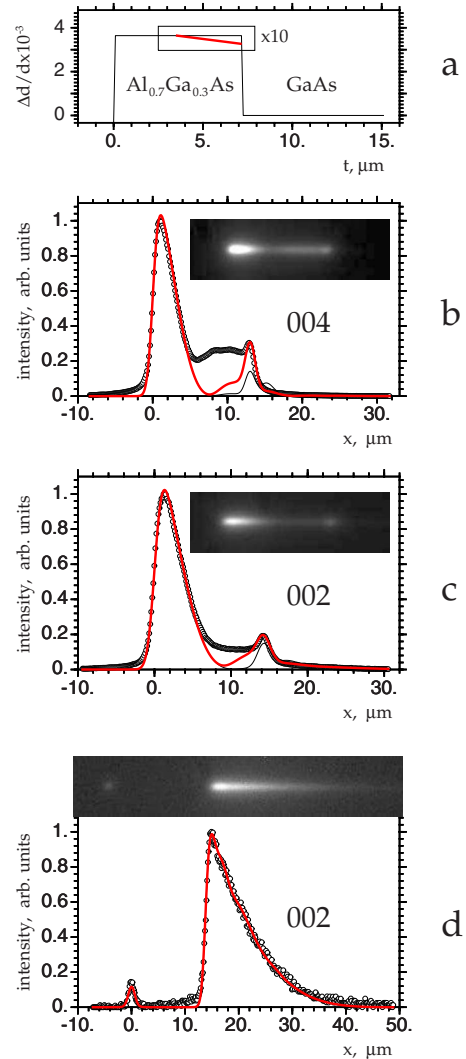


FIG. 4. (Color online) (a) Schematics of the MBE grown $Al_{0.7}Ga_{0.3}As$ epitaxial film on GaAs(001) substrate: film with uniform composition (thin line) and with a small gradient in the second half of the film (thick line, red); [(b)–(d)] central cross sections of the diffraction images (shown as insets) for different diffraction conditions: (b) (004) and (c) (002) reflections, diffraction peak from the film is within the angular aperture of the zone plate; (d)—(002) reflection, diffraction peak from the substrate is within the angular aperture of the zone plate. Open circles experiment, solid lines—theoretical calculations for uniform film (thin line) and the film with the gradient (thick line, red).

include the relative shift of the Bragg angle and the static Debye-Waller (DW) factor. In this way, complex multilayer semiconductor structures and crystals with compositional and lattice-constant profiles can be modeled. It was found that introduction of a small gradient in the film can significantly improve the fit. The profile providing the best fit corresponds to the total relative Bragg angle shift of only $30 \mu rad$ toward the interface. This part of the film was modeled by introducing 40 sublayers with the $\Delta d/d$ profile shown in Fig. 4(a) (enhanced by ten times for clarity) as a thick (red) line. The intensity distributions calculated for this profile are shown by thick (red) lines on the intensity profiles

in Fig. 4. As one can see, the agreement with theory in the interface region is now significantly improved demonstrating high sensitivity of this technique to very small structural details.

Additional intensity between the peaks in Figs. 4(b) and 4(c) is still very strong and cannot be described within the perfect-crystal model. This fact, however, has a clear physical interpretation. It is well known¹⁵ that for an epitaxial mismatched film with the thickness above a certain critical value the strain accumulated in the film is relaxed through the generation of dislocations at the interface. Multiplication of dislocations and their interaction with point defects lead to complex defect structures inside the film. X-ray rocking curve measurements combined with reciprocal-space mapping¹⁶ give an estimate of the density of the threading dislocation segments of $3.0 \times 10^6 \text{ cm}^{-2}$. It is reasonable to explain the enhanced intensity that we observe in our images with the presence of defects in the film.

The images shown in Fig. 4 demonstrate also that the diffraction contrast and the sensitivity to defect structure strongly depend on diffraction conditions. The images in Figs. 4(b) and 4(c) were taken at the angular positions which correspond to the diffraction peak from the film. The peak from the surface layer is stronger than the peak from the interface. Since the film is thicker than the extinction length the part of the images below the extinction depth are very sensitive to the defect structure. The image in Fig. 4(d) is taken at the angle which corresponds to the diffraction peak from the substrate. Even if the film is outside the zone-plate aperture the peak from the film is still visible though it is not so sensitive to the structural details. The peak from the substrate is formed by extinction and it is similar to the one shown in Fig. 3(b). Using this reflection the thickness of the film can be measured very accurately.

B. AlGaAs multilayer on GaAs(001)

A more complex multilayer structure is shown schematically in Fig. 5(a). It consists of five layers; each has a compositional profile in the form of a symmetrical trapezoid and separated from the neighbors by thin buffer GaAs layers. On the (002) x-ray rocking curve the multilayer as a whole shows as a separate diffraction peak shifted by -1.6 mrad from the substrate GaAs(002) peak. Two (002) diffraction images and intensity profiles are shown in Fig. 5. First image shown in Fig. 5(b) was taken at the diffraction position which corresponds to the peak from the film; the second one, Fig. 5(c), corresponds to the peak from the substrate.

The diffraction image on Fig. 5(b) shows five distinctive peaks, which correspond to the five layers of the multilayer structure. At this angle the substrate is off the Bragg condition and not visible on the image. On the image in Fig. 5(c) six diffraction spots are observed. Now the substrate is at the Bragg angle and it shows as a strong peak slowly decaying with depth similar to Figs. 3(b) and 4(c).

For computer simulations each layer was modeled by five sublayers, two on each side with the zero Bragg angle shift for the buffer layers and three layers with -1.58 , -1.67 , and -1.58 mrad Bragg shifts for the compositional profile in the

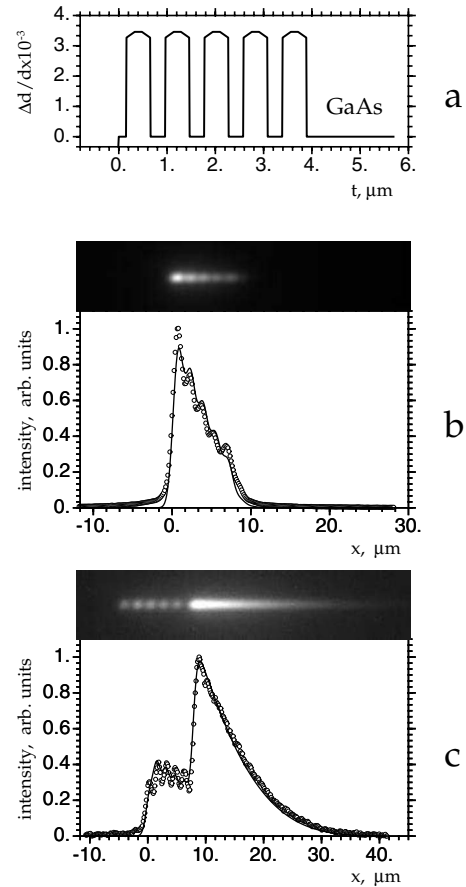


FIG. 5. (a) Schematics of the five-layer AlGaAs semiconductor structure of a complex compositional profile grown by MBE on GaAs(001) substrate; [(b) and (c)] central cross sections of the (002) diffraction images (shown as insets) taken at the angular positions corresponding to the multilayer peak (b) and the substrate peak (c); open circles experiment, solid line-computer simulations for a simplified model of the uniform within each layer composition profile.

center. The total number of layers including substrate was 26. Theoretical curves are shown in Figs. 5(b) and 5(c) as solid lines. Interestingly enough, the visibility of the diffraction peaks on the calculated curves is lower than in the experiment. Obviously, the approximation of the compositional gradient by only one layer is too coarse. This fact confirms very high sensitivity of the technique to the structural details. Unfortunately, more accurate simulation requires a number of layers that at present cannot be handled easily on an ordinary PC [compositional gradient shown in Fig. 4(a) was approximated by 40 sublayers]. However, the thickness of the multilayer can be determined very accurately: the best fit gives the total thickness of $4.05 \mu\text{m}$.

VI. IMAGING DEFECTS IN ANNEALED Si CRYSTAL

In this section we present experimental images obtained from bulk defects in silicon. The defects were created by annealing a Czochralski grown Si wafer for 4 h at 1050 C in N_2 . It is known that during such annealing oxygen atoms

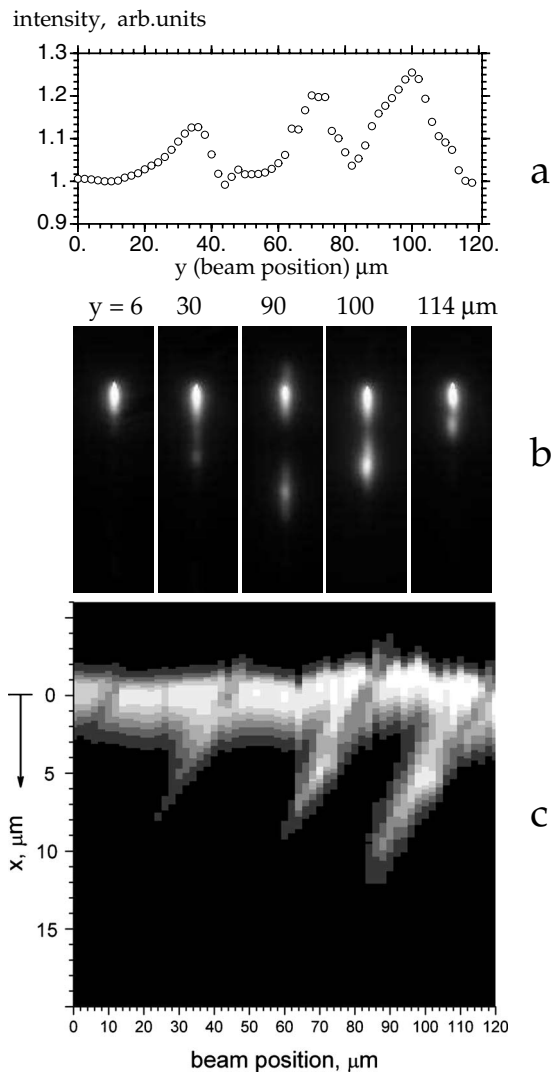


FIG. 6. Visualization of individual defects in a nearly perfect Si crystal by scanning the crystal in the focused beam. (a) Integrated CCD intensity as a function of the beam position. (b) Individual (111) diffraction images for five selected beam positions. (c) Two-dimensional intensity map of the defect region composed from cross sections through the individual diffraction images.

precipitate in the form of silica leading to formation of rods, disks, dislocation loops, and stacking faults.¹⁷ After annealing, the sample was etched to remove any possible surface damage. The diffraction images were taken at a fixed Si(111) Bragg angle while scanning the sample perpendicular to the diffraction plane with the step of 2 μm. Total intensity over all CCD pixels was displayed on a monitor screen. Perfect regions produce images similar to the one shown in Fig. 2(a) with a constant CCD intensity. Any increase in the total intensity level indicates the presence of defects within the area illuminated by the focused beam.

Figure 6(a) shows the part of the scan with three regions of increased intensity. Examination of the individual images revealed additional intensity spots originating from the bulk of the sample. Some of these images are shown in Fig. 6(b) for different values of the relative beam position. As the scan proceeds the spot moves toward the surface and then disap-

pear [last three images in Fig. 6(b)]. A two-dimensional intensity map composed from the cross sections through all subsequent diffraction images is shown in Fig. 6(c). The surface is located around $x=0$. As one can see, all three features in Fig. 6(c) have a very similar shape. We may assume therefore that they originate from the individual defects or defect aggregations of a similar nature.

We are not able to identify exactly what kind of defects generate these images because a very low defect density makes electron microscope analysis problematic. We may speculate that this may be a thin silica rod or a platelet formed by the oxygen precipitation lying in a certain crystallographic plane and inclined to the surface. The defect breaks up the destructive interference field in the bulk and shows as a spot of an additional intensity with the position of the spot indicating the depth at which diffraction plane intersects the defect. The spot disappears as the defect approaches the surface.

VII. DISCUSSION AND CONCLUSIONS

In previous sections we presented experimental images obtained with a new diffraction imaging technique based on a focused x-ray beam. We demonstrated that when applied to perfect single crystals, this scheme can be used to study the formation of x-ray fields inside the crystal and experimentally measure extinction length in a direct way. It opens up interesting possibilities for new experiments in x-ray diffraction physics. We already mentioned one of them—to study how extinction length changes with energy through absorption edges. Another interesting problem is to study the effect of crystal perfection on extinction. The static Debye-Waller factor $e^{-W_{st}}$ describing the average displacement of atoms from their regular positions in the lattice caused by defects enters the expression for the extinction length directly through $|\chi_h|$. Introducing point defects by, for instance, uniformly irradiating crystal with neutrons or high-energy electrons, one can change the static DW factor in a controllable way. The annealing of irradiated crystals will produce dislocation loops with their size depending on the annealing conditions. The direct measurements of extinction lengths in crystals with defects, combined with the measurements of the diffuse scattering, will help to validate developed recently theoretical dynamical scattering models.¹⁸

Experimental images recorded from epitaxial films and multilayers prove high depth sensitivity. We showed that any interface between two layers of different lattice constant or composition generates a phase shift that can change the phase relationship of the x-ray fields inside the crystal and produce contrast. We demonstrated a very high sensitivity of the technique to even small compositional gradients. Thickness of the layer can be measured with high accuracy either by simply measuring the spatial distance between the peaks from the front and the back surfaces of the layer or performing computer simulations.

The technique described here can be viewed as an alternative solution to perform sectional topography in the Bragg case. Indeed, due to the experimental difficulties described in Sec. I, the closest approximation to the section topography in

the Bragg case is a Berg-Barrett technique, see Refs. 1 and 14, and references therein. In this technique, a narrow x-ray beam with the size of about few tens of microns is incident at a small angle to the surface of a crystal, Bragg diffracted by means of an asymmetric reflection and recorded on a film or a CCD detector placed a few millimeter from the crystal parallel to the surface. The technique provides sensitivity to structural defects in thin surface layers with the thicknesses determined by the extinction and the penetration depths at grazing incident angles. The depth sensitivity is achieved by tuning the penetration depth, typically in the range from few microns to tens of microns and more (e.g., see Ref. 19), by changing the incident angle within the Darwin width of the rocking curve. Another approach, section Bragg topography on thick Si crystals with the thickness of several millimeter was demonstrated in Ref. 20 based on using high-energy x rays and high-order reflections. It was shown that the depth of bulk defects (together with their sizes and density) can be determined from the topographic images. This approach, however, lacks surface sensitivity, which is important for many applications.

Our technique does not have these limitations. It can be used with any x-ray energy and all reflections available from the crystal. The depth resolution, i.e., the sharpness of the contrast, is determined by the size of the beam in the focus, which can be as small as a few tens of nanometer. The resolution is currently limited by the detector: the spatial resolution of the best CCD cameras is currently about 1 μm . The theoretical limit for x-ray-to-light technologies is 0.3 μm (Ref. 21) but improvements even by a factor of 2 presents huge challenges. Because of a one-dimensional nature of our images imposed by diffraction, the knife-edge scan, which is routinely used today for measuring the smallest focused beams, is always an option.

One of the advantages of our technique is the zooming possibility: since the sample can be positioned anywhere be-

tween the focusing optics and focus, the size of the illuminating area can be easily controlled by simply translating the sample along the optical axis. In the setup shown in Fig. 1 this freedom is limited by the distance between the OSA and the focus. With the refractive lenses which do not require OSA (or any other additional elements) the size of the beam incident on the sample can be varied from roughly the lens aperture, typically 20–40 μm , to the smallest distance to the detector determined by the sample size. Consider as an example a setup with two crossed planar lenses with the focal distance of about 100 mm producing the focused beam of 100 nm \times 100 nm.²² Then, with the sample-to-detector distance of 0.5 mm the lateral size of the illuminated area on the sample could be as small as 200–250 nm, which will determine the lateral resolution of our technique. It can be used to study the structural variations across submicrometer size devices or to investigate the strain fields around individual defects in crystals. The depth sensitivity can be greatly enhanced by using kinematical diffraction, i.e., taking diffraction images at the incident angles outside the focusing optics aperture.^{9,10}

ACKNOWLEDGMENTS

The authors thank Nikolai Faleev for growing epitaxial film and multilayer structures and helpful discussion. This work is based upon research conducted at the Cornell High Energy Synchrotron Source (CHESS) which is supported by the National Science Foundation and the National Institutes of Health/National Institute of General Medical Sciences under NSF Award No. DMR-0225180. The work of V.G.K. was supported by RFBR under Grants No. 09-02-12297-ofi_m and No. RS-4110.2008.2. Use of the Advanced Photon Source was supported by the U.S. Department of Energy, Office of Science, Office of Basic Energy Sciences, under Contract No. DE-AC02-06CH11357.

*ayk7@cornell.edu

¹A. Autier, *Dynamical Theory of X-Ray Diffraction* (Oxford University Press, New York, 2001).

²T. Uragami, *J. Phys. Soc. Jpn.* **27**, 147 (1969); **28**, 1508 (1970); **31**, 1141 (1971).

³A. M. Afanas'ev and V. G. Kohn, *Acta Crystallogr., Sect. A: Cryst. Phys., Diffr., Theor. Gen. Crystallogr.* **27**, 421 (1971).

⁴T. Saka, T. Katagawa, and N. Kato, *Acta Crystallogr.* **A28**, 102 (1972); **A28**, 113 (1972); **A29**, 192 (1973).

⁵V. G. Kohn, *Crystallogr. Rep.* **51**, 564 (2006).

⁶V. G. Kohn and A. Kazimirov, *Phys. Rev. B* **75**, 224119 (2007).

⁷A. Kazimirov, V. G. Kohn, and Z.-H. Cai, *Proc. SPIE* **7077**, 70770L (2008).

⁸A. Kazimirov, V. G. Kohn, and Z.-H. Cai, *J. Phys. D* **42**, 012005 (2009).

⁹A. Kazimirov, V. G. Kohn, A. Snigirev, and I. Snigireva, *J. Synchrotron Radiat.* **16**, 666 (2009).

¹⁰A. Kazimirov, V. G. Kohn, A. Snigirev, and I. Snigireva, *Proc. SPIE* **7448**, 74480P (2009).

¹¹Y. Xiao, Z. Cai, Z. L. Wang, B. Lai, and Y. S. Chu, *J. Synchrotron Radiat.* **12**, 124 (2005).

¹²V. G. Kohn, Yu. V. Shvydko, and E. Gerdau, *Phys. Status Solidi*

B **221**, 597 (2000).

¹³B. W. Batterman, *Phys. Rev.* **133**, A759 (1964).

¹⁴D. K. Bowen and B. K. Tanner, *High Resolution X-Ray Diffractometry and Topography* (Taylor & Francis, London, 2002).

¹⁵J. W. Matthews and A. E. Blakeslee, *J. Cryst. Growth* **27**, 118 (1974).

¹⁶N. Faleev (private communication).

¹⁷J. I. Schneider, O. D. Goncalves, A. J. Rollason, U. Bonze, J. Lauer, and W. Zulehner, *Nucl. Instrum. Methods Phys. Res. B* **29**, 661 (1988).

¹⁸V. B. Molodkin, S. I. Olikhovskii, E. N. Kislovskii, T. P. Vladimirova, E. S. Skakunova, R. F. Seredenko, and B. V. Sheludchenko, *Phys. Rev. B* **78**, 224109 (2008).

¹⁹Y. Zhong, S. Krasnicki, A. T. Macrander, Y. S. Chu, and J. Maj, *J. Phys. D* **38**, A39 (2005).

²⁰S. Iida, R. Kitamura, T. Abe, and H. Kawata, *Jpn. J. Appl. Phys., Part 1* **38**, 2845 (1999).

²¹A. Koch, C. Raven, P. Spanne, and A. Snigirev, *J. Opt. Soc. Am. A* **15**, 1940 (1998).

²²A. Snigirev, I. Snigireva, M. Grigoriev, V. Yunkin, M. Di Michiel, S. Kuznetsov, and G. Vaughan, *Proc. SPIE* **6705**, 670506 (2007).